

# Fusion of Charged Block Copolymer Micelles into Toroid Networks

Stephan Förster,\* Nadja Hermsdorf, Walter Leube, Heimo Schnablegger, Mathias Regenbrecht, and Sabri Akari

Max-Planck-Institut für Kolloid- und Grenzflächenforschung, Am Mühlenberg, D-14424 Potsdam-Golm, Germany

Peter Lindner

Institut-Laue-Langevin, F-38042 Grenoble Cedex 9, France

Christoph Böttcher

Freie Universität Berlin, Institut für Organische Chemie, Takustrasse 3, D-14195 Berlin, Germany

Received: January 6, 1999; In Final Form: May 24, 1999

The association behavior of polyelectrolyte block copolymers in aqueous solution as a function of polymer and salt concentration is investigated for poly(ethylene-*b*-styrenesulfonic acid) (PEE-PSSH). This copolymer combines a soft hydrophobic block with a highly charged polyelectrolyte block that allows direct dissolution in aqueous solutions to investigate micellization under equilibrium conditions. Increasing polymer and salt concentration leads to the fusion of polyelectrolyte micelles into vesicles and fractal toroid-micronetworks. Association structures were characterized by static light scattering (SLS), small-angle neutron scattering (SANS), transmission electron microscopy (TEM), and atomic force microscopy (AFM). At high salt concentrations the solution phase separates into a dilute micellar phase and a concentrated gel phase.

## 1. Introduction

Block copolymers consisting of a hydrophobic block and a polyelectrolyte block have structural features of polyelectrolytes, block copolymers, surfactants, and filamentous proteins like proteoglycans. Their self-assembly behavior can be imagined to be of unusual complexity because of the interplay between packing and charge effects. A basic knowledge of their modes of self-assembly and their correspondence to application-related properties (drug delivery, polymeric emulsifiers) is just now being developed and poses a considerable scientific challenge.

Surfactants are known to self-assemble into a variety of different structures (spheres, cylinders, bilayers) depending on molecular shape, temperature, or concentration. In dilute solution they form micelles very much like block copolymers in selective solvents. Micellization of uncharged block copolymers has been well investigated.<sup>1,2</sup> In contrast, relatively few studies on the micellization of charged block copolymers in aqueous solutions have appeared<sup>3–5</sup>. Experimental investigations have been restricted by the unusually low solubility of most polyelectrolyte block copolymers in water. Direct dissolution is in most cases impossible, even for large polyelectrolyte blocks.<sup>3</sup> The dispersion of the solid polymer in water requires to break up hydrophobic domains. Because these domains are in most cases glassy (e.g. in the case of polystyrene), thermal energy is insufficient for spontaneous dissolution.

It has become a standard technique for the preparation of aqueous polyelectrolyte block copolymer solutions to first dissolve the polymer in a common polar organic solvent such as DMF, dioxane, or THF. Then water is added to induce micelle formation. The organic solvent is then removed by dialysis. During the dialysis procedure micellar cores completely segregate from the aqueous medium and become glassy. The

exchange of polymers between micelles, which is necessary to sustain thermodynamic equilibrium, will eventually cease, leading to the formation of “frozen micelles”. The disappearance of the micellar equilibrium can be followed by sedimentation velocity<sup>6</sup> and electron microscopy<sup>7</sup>. As expected for “frozen” metastable states, thermodynamic properties such as aggregation numbers and polydispersities in aqueous solutions were found to depend on the sample preparation procedure.<sup>8</sup>

Although representing a non-equilibrium state, studies on “frozen” micelles have provided valuable insights, e.g., into micellar take-up and release of organic molecules.<sup>9–12</sup> Particularly revealing have been recent studies by the group of Eisenberg et al. who demonstrated that a multitude of different micellar shapes (spheres, cylinders, vesicles, compound vesicles) exists for charged crew-cut block copolymer micelles.<sup>13–19</sup> The morphologies seem to depend on the degree of charge repulsion in the micellar corona which can be influenced by block lengths, ionic strength, and solvent composition.

So far, only a few studies considered polyelectrolyte block copolymers that are directly soluble in water which allows to investigate micellar structures under thermodynamic equilibrium. An example for such a block copolymer is poly(*tert*-butylstyrene-*b*-styrenesulfonate) with short hydrophobic segments. Micellization was investigated by rheology,<sup>20</sup> fluorescence,<sup>21</sup> static and dynamic light scattering (SLS, DLS), and small-angle neutron scattering (SANS).<sup>22,23</sup> A decrease of the measured hydrodynamic radius  $R_h$ , radius of gyration  $R_g$ , and aggregation number  $Z$  with increasing salt concentration was observed. For a larger hydrophobic block, SLS and DLS showed a bimodal distribution of micelles with  $R_h \approx 40$  nm and large aggregates with a size of  $R_h \approx 600$  nm<sup>24</sup> whose origin was unclear.

These studies show the possibility to investigate micellar

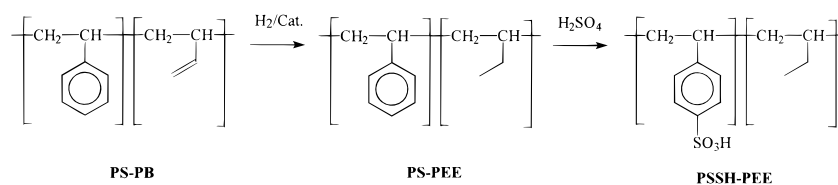


**Figure 1.** Synthesis route for poly(styrenesulfonicacid-*b*-ethylethylene) (PSSH-PEE) block copolymers via catalytic hydrogenation of poly(styrene-*b*-butadiene) (PS-PB) followed by sulfonation of poly(styrene-*b*-ethylethylene) (PS-PEE).

equilibrium properties using directly water-soluble polyelectrolyte block copolymers. The observed bimodal distribution of micellar sizes indicates some more complicated association behavior, possibly related to the observations by the group of Eisenberg et al. In the present work we investigate a directly water-soluble polyelectrolyte block copolymer poly(ethylethylene-*b*-sulfonic acid) (PEE-PSSH) with a large hydrophobic block in order to study possibly complex association behavior. Association structures are characterized by a combination of scattering (SLS, SANS) and microscopy techniques (TEM, AFM). During the course of our work, AFM developed into an ambitious tool for imaging complex association structures. Therefore the extensive AFM studies were put into a separate report following the present paper.<sup>25</sup> The observed association behavior is put into the framework of concepts developed for low molecular weight surfactants.

## 2. Experimental Part

**2.1. Block Copolymer Synthesis. Anionic polymerization.** Poly(styrene-*b*-butadiene) (PS-PB) was synthesized by anionic polymerization following standard vacuum line procedures. Styrene was purified from  $\text{LiAlH}_4$  and  $n\text{-Bu}_2\text{Mg}$ , butadiene from  $n\text{-Bu}_2\text{Mg}$  and  $n\text{-BuLi}$ , and THF from Na/K alloy and K-benzophenone complex. Polymerization was initiated with a calculated amount of *s*-BuLi (1.3 *m* solution in hexane) which was injected to the styrene/THF solution just above its melting point ( $-110^\circ\text{C}$ ). The solution is kept at  $-78^\circ\text{C}$  for 30 min to complete polymerization. A sample of the PS block is withdrawn for polymer analysis. Then the calculated amount of butadiene is cryodistilled into the reactor over a period of 1 h. The polymerization of butadiene takes 5–6 h at  $-78^\circ\text{C}$ . The PS-PB block is quenched with degassed methanol, precipitated in a methanol/isopropanol mixture, and dried to constant weight under vacuum.

The molecular weight of the PS-precursor and the polydispersity of the PS-PB block was determined by GPC in THF calibrated with narrow PS standards. The block copolymer composition was calculated from the ratio of aromatic and olefinic resonances in  $^1\text{H-NMR}$ . From the olefinic peaks, a relative amount of 89.5% 1,2-addition to 19.5% 1,4-addition were determined in agreement with literature data.<sup>26</sup> According to our analysis, the degrees of polymerization are  $N(\text{PB}) = 114$  and  $N(\text{PS}) = 83$  with a polydispersity of the PS precursor of  $M_w/M_n = 1.03$  and of the PS-PB block copolymer of  $M_w/M_n = 1.04$ .

**Catalytic Hydrogenation.** The PB block was hydrogenated using Wilkinson's catalyst ( $\text{RhCl}(\text{PPh}_3)_3$ ).<sup>27</sup> Typically, 10 g of PS-PB are dissolved in 100 mL of dry toluene, to which  $\text{RhCl}(\text{PPh}_3)_3$  and  $\text{PPh}_3$  in 50 mL toluene are added in a 1/100 and 3/100 molar ratio to butadiene, respectively. The reaction is carried out in a stirred 200 mL autoclav (Berghof) at  $120^\circ\text{C}$  and a hydrogen pressure of 25–30 bar for 5 h. After hydrogenation, toluene is removed by distillation and the polymer is

refluxed in acetone to extract the catalyst via formation of a Rh-acetonate complex. The polymer is removed by filtration, then redissolved in THF/acetone, precipitated in methanol, and dried under vacuum. GPC showed no noticeable changes of the molecular weight distribution after hydrogenation. Complete saturation ( $>99\%$ ) was achieved according to  $^1\text{H-NMR}$ .

**Sulfonation.** The PS-block was sulfonated with 3-fold excess acetyl sulfate in dichloroethane at  $60^\circ\text{C}$ .<sup>28</sup> Acetyl sulfate was freshly prepared by reacting sulfuric acid with acetic anhydride. Typically 10 g of PS-PEE are dissolved in 200 mL dichloroethane and acetylsulfate in dichloroethane is added under stirring at  $60^\circ\text{C}$ . After 2–3 h, the sulfonated polymer precipitates and is removed by filtration. The polymer is further purified from traces of sulfuric acid and acetic acid by dissolution in methanol and precipitation in diethyl ether. The degree of sulfonation, as determined by  $^1\text{H-NMR}$  from the aromatic peak ratios, is 80%. The polymer obtained by this procedure does not contain low molecular weight ionic impurities, and further purification by ultrafiltration has been found to be unnecessary. We have found that more reactive sulfonating agents like  $\text{H}_2\text{SO}_4/\text{P}_2\text{O}_5$ <sup>29</sup> lead to higher degrees of sulfonation but also to side reactions causing broadening of the molecular weight distribution. The synthesis route of the block copolymer is summarized in Figure 1.

**2.2. Structure Analysis. Sample Preparation.** Polymers were directly dissolved in aqueous salt solutions. Complete dissolution can take up to 48 h at the highest salt concentrations ( $c_s > 1$  mol/L) at room temperature. At elevated temperatures ( $T = 70^\circ\text{C}$ ), sample preparation takes 12 h (overnight). It was checked that the sample properties did not depend on the sample preparation procedure. The use of ultrasonic treatment was found to be unnecessary. For further analysis, the solutions were filtered through 0.8 or  $0.45\ \mu\text{m}$  Millipore filters. The pore size becomes an issue at high salt concentration, where large polyelectrolyte association structures are lost upon filtration when using too small pore sizes.

**Light Scattering.** Light-scattering experiments were carried out at  $20.0^\circ\text{C}$ . A commercial spectrometer from ALV (Langen, Germany), consisting of an ALV ISP86 goniometer and an ALV 5000 multi- $\tau$  correlator, was used. The measurements were performed using the  $\lambda = 532\ \text{nm}$  line of a cw frequency doubled, diode pumped Nd:YAG laser (ADLAS 425c) with 300 mW output power. The refractive index increment was determined using a scanning interferometric refractometer (NFT scan). The measured increment was  $dn/dc = 0.169\ \text{cm}^3/\text{g}$ . Toluene with an absolute scattering power of  $I_{\text{std}} = 2.662 \times 10^{-5}\ \text{cm}^{-1}$  was used for calibration to determine the scattering volume corrected Rayleigh ratio as

$$I_R(q) = \frac{I_{\text{sol}}(q) - I_{\text{svt}}}{I_{\text{tol}}} I_{\text{std}} \left( \frac{n_{\text{sol}}}{n_{\text{tol}}} \right)^2 \quad (1)$$

where  $I_{\text{sol}}$  is the scattering intensity of the solution,  $I_{\text{svt}}$  the scattering intensity of the solvent (water), and  $I_{\text{tol}}$  the scattering intensity of toluene. The scattering vector is defined as  $q =$

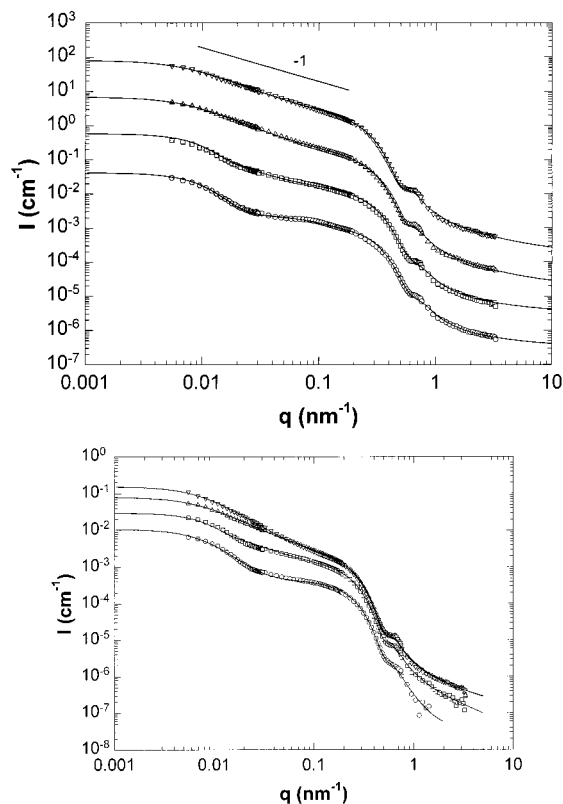


**Figure 2.** SLS/SANS scattering curves for different salt concentrations  $c_s = 0.001$  (○),  $0.01$  (□),  $0.1$  (△), and  $1$  mol/L (▽) at a polymer concentration of (a)  $c_p = 6$  g/L and (b) for different polymer concentrations  $c_p = 1$  (○),  $3$  (□),  $6$  (△), and  $10$  g/L (▽) at a salt concentration of  $c_s = 1$  mol/L. With increasing ionic strength there is a build-up of scattering intensity at low and intermediate  $q$  values indicating the fusion of micelles into larger association structures. Grey-filled symbols denote SLS data. Solid lines are nonlinear least-squares fits. The straight line denotes a slope of  $q^{-1}$ .

$(4\pi n/\lambda) \sin(\vartheta/2)$ , where  $n$  is the refractive index of the solution and  $\vartheta$  the scattering angle. The relation between scattered intensity and particle structure is given by

$$I(q) = k c M P(q) S(q) \quad (2)$$

where  $k$  is the contrast factor (in  $[\text{cm}^2 \text{ mol/g}^2]$ ),  $c$  the polymer concentration (in  $[\text{g/cm}^3]$ ),  $M$  the molecular weight (in  $[\text{g/mol}]$ ),  $P(q)$  the form factor, and  $S(q)$  the structure factor. The factorization  $P(q)S(q)$  is an approximation which is exact for spherical, monodisperse particles. The light scattering contrast factor is given by  $k = [(4\pi^2 n^2)/(N_L \lambda^4)](dn/dc)^2$ .

At low salt concentration, electrostatic interactions can influence the scattering behavior considerably. These interactions lead to so-called “polyelectrolyte effects” that include positional correlations, low- $q$  upturns in the scattering curves, and the observation of a slow mode in dynamic light scattering.<sup>30</sup> These phenomena occur at a ratio of polyelectrolyte (monomer) to salt concentration of  $\lambda^* = c_p/c_s > 1$  for linear flexible polyelectrolyte chains.<sup>31</sup> They complicate the determination of size and shape of dissolved particles. This implies that investigations of single particle properties at low salt concentrations of  $0.01$  or  $0.001$  mol/L require to study polymer concentrations below  $2$  or  $0.2$  g/L, respectively. Advantageously, for dense polyelectrolyte structures like stars, spheres, or brushes, charge renormalization shifts the ratio  $\lambda^*$  to larger values  $\lambda^* \gg 1$ , which allows us to work at larger polymer concentrations. In our case the sample with the lowest amount of added salt ( $c_s = 0.001$  mol/L at  $c_p = 6$  g/L) has the largest value of  $\lambda^* = 25$ . We

could neither observe a low- $q$  upturn, a slow-mode, nor a minimum (Figure 2) in the scattering curves indicating that the added salt concentration is sufficiently high to screen intermolecular electrostatic interactions.

**Small-Angle Neutron Scattering.** The measurements were performed at the 20, 5, and 1.1 m detector position at the D11 small-angle instrument at ILL, Grenoble. The neutron wavelength was  $\lambda = 0.6$  nm with a relative standard deviation of  $\Delta\lambda/\lambda = 9\%$  (FWHM). Details of the instrumentation and data reduction can be found elsewhere.<sup>32</sup> The scattering intensity was put on absolute scale by calibration with water. The neutron contrast factor is defined as

$$k = (\Delta b)^2/N_L \quad (3)$$

where  $\Delta b$  is the contrast between polymer and solvent and  $N_L$  Avogadro’s number. The contrast  $\Delta b$  is given by

$$\Delta b = \left[ \frac{N_L \sum_i b_{2,i}}{m_2} - \frac{v_2}{v_1} \frac{N_L \sum_i b_{1,i}}{m_1} \right] \quad (4)$$

where the  $b_{ij}$  values are the atomic scattering cross sections of atom  $j$  in the solvent ( $i = 1$ ) and in the monomer unit ( $i = 2$ ) (in  $[\text{cm}]$ ),  $m$  are the molecular weights of the solvent and monomer (in  $[\text{g/mol}]$ ), and  $v$  are the partial specific volumes (in  $[\text{cm}^3/\text{g}]$ ). To a first approximation,  $v = 1/\rho$  can be used, where  $\rho$  is the bulk density (in  $[\text{g/cm}^3]$ ). The total scattering contrast of the block copolymer is calculated to be  $k = k_{\text{PEE}}N_{\text{PEE}} + k_{\text{PSSD}}N_{\text{PSSD}} = 1.343 \text{ cm}^2 \text{ mol/g}^2$  with a total molecular weight of  $m_{\text{PEE}}N_{\text{PEE}} + m_{\text{PSSD}}N_{\text{PSSD}} = 21770 \text{ g/mol}$ .

**Form Factor Analysis.** To obtain a continuous set of scattering curves over a large  $q$ -range, the SLS-curves were shifted vertically by a constant factor approximately (within 10%) equal to the ratio of contrast factors to overlap with the SANS-curves from the 20 m detector position. The slope in the overlapping  $q$ -range was the same for SLS and SANS. Measured scattering curves were fitted by a nonlinear least-squares method using the Levenberg–Marquardt algorithm. The form factors considered in the present study are summarized in Table 1.  $R$  corresponds to the radius of a sphere or the cross-sectional radius of a cylinder.  $L$  is the cylinder length,  $J_1(z)$  the Bessel function,  $\text{Si}(z)$  the sine integral,  $d$  the fractal dimension, and  ${}_0F_1(q,R)$  and  ${}_1F_2(q,a,R)$  denote hypergeometric functions. The factorization of the cylinder form factor is a good approximation for long cylinders, where  $L > 10R$ . The derivation of  $P_s(q)$  is explained in the Appendix. The form factor of the micelle assumes a constant (scattering) density profile  $b = b_c$  in the micellar core of radius  $R_c$  and a hyperbolic  $b(r) = b_s(r/R_c)^{-a}$ -profile in the shell, i.e., in the regime  $R_c < r \leq R_m$ , where  $R_m$  is the outer radius of the micelle.<sup>33</sup> Such a profile was derived for star polymers<sup>34</sup> and has been shown to adequately describe the structure of strongly segregated block copolymer micelles.<sup>35</sup> The radius of gyration of the micelle is obtained from

$$R_g^2 = \frac{\frac{b_1}{5} + \frac{b_2}{5+a}(p_1^{-(5+a)} - 1)}{\frac{b_1}{3} + \frac{b_2}{3+a}(p_1^{-(3+a)} - 1)} p_1^2 R_m^2$$

where  $p_1 = R_c/R_m$ . Polydispersity is taken into account by

**TABLE 1: Form factors of spheres  $P_{\text{sph}}(q)$ , fractal aggregates  $P_{\text{frac}}(q)$ , spherical micelles  $P_{\text{mic}}(q)$ , fluctuations  $P_{\text{fluc}}(q)$ , and cylinders  $P_{\text{cyl}}(q)$  used for the analysis of the SLS/SANS-curves**

particle	form factor	
sphere	$P_{\text{sph}}(q) = \frac{9}{(qR)^6}(\sin(qR) - qR \cos(qR))^2$	$R$ = sphere radius
fractal	$P_{\text{frac}}(q) = (1 + N_{\text{frac}}P_s(q))P_{\text{sph}}(q)$ $P_s(q) = \frac{\sin[(d-1)\arctan(X)]}{(d-1)X[1 + X^2]^{(d-1)/2}}$	$N_{\text{frac}}$ = number of spheres $X = \frac{qR_g}{\sqrt{d(d+1)}}$ $R_g$ = radius of gyration $d$ = fractal dimension
micelle	$P_{\text{mic}}(q) = \left( \frac{\frac{b_c}{3} F_1\left(\frac{3}{2}, -\frac{q^2 R_c^2}{4}\right) - \frac{b_s}{3-a} F_2\left(\frac{3-a}{2}, \frac{3}{2}, \frac{5-a}{2}, -\frac{q^2 R_c^2}{4}\right) + \left(\frac{R_c}{R_m}\right)^{a-3} \frac{b_s}{3-a} F_2\left(\frac{3-a}{2}, \frac{3}{2}, \frac{5-a}{2}, -\frac{q^2 R_m^2}{4}\right)}{\frac{b_c}{3} - \frac{b_s}{3-a} + \left(\frac{R_c}{R_m}\right)^{a-3} \frac{b_s}{3-a}} \right)^2$	$R_c$ = core radius $R_m$ = micellar radius $b_c$ = core contrast factor $b_s$ = shell contrast factor $a$ = exponent $\xi$ = correlation length
fluctuations	$P_{\text{fluc}}(q) = \frac{2}{q\xi} \text{Si}(q) - \left( \frac{\sin(q\xi/2)}{q\xi/2} \right)^2$	
cylinder	$P_{\text{cyl}}(q) = \left( \frac{2}{qL} \text{Si}(q) - \left( \frac{\sin(qL/2)}{qL/2} \right)^2 \right) \left( \frac{2J_1(qR)}{qR} \right)^2$	$L$ = cylinder length $R$ = cylinder radius

averaging over a Schulz–Zimm distribution

$$P_x(q) = \int_0^\infty P(q,R)h(R)dR$$

$$h(R) = \frac{(z+1)^{z+1} R^z}{\langle R \rangle^{z+1} \Gamma(z+1)} \exp\left[-\frac{(z+1)R}{\langle R \rangle}\right] \quad (5)$$

with the average radius  $\langle R \rangle$  and the relative standard deviation  $\sigma = (z+1)^{-1/2}$ .

**Transmission Electron Microscopy.** TEM was performed on a 100 kV Phillips electron microscope. Samples were cast on uncoated Cu grids and negatively stained with uranyl acetate.

### 3. Results and Discussion

**3.1. Light and Neutron Scattering.** The measured scattering curves for different polyelectrolyte and salt concentrations are shown in Figure 2. The scattering curves undergo a characteristic change with increasing ionic strength. At low ionic strength a pronounced decrease of the scattering intensity at low  $q$  ( $0.005 \leq q \leq 0.03 \text{ nm}^{-1}$ ) is followed by a plateau region with nearly constant scattering intensity ( $0.03 < q \leq 0.2 \text{ nm}^{-1}$ ). Above  $q = 0.2 \text{ nm}^{-1}$  the scattering curve exhibits damped oscillations with a  $q^{-4}$  Porod envelope until at large  $q$  ( $q > 1 \text{ nm}^{-1}$ ) it enters a regime of slow decay into the base line. Increasing the ionic strength primarily affects the scattering curve at low  $q$  ( $q < 0.2 \text{ nm}^{-1}$ ), where a pronounced overall increase of the scattering intensity is accompanied by a built-up of a characteristic  $q^{-1}$  dependence over nearly 2 orders of magnitude in the scattering vector ( $0.005 \leq q \leq 0.2 \text{ nm}^{-1}$ ).

The scattering curves at low ionic strength are typical for coexisting small ( $R \approx 10 \text{ nm}$ ) and large ( $R \approx 200 \text{ nm}$ ) globular structures. With increasing ionic strength they evolve into scattering curves characteristic for large self-similar structures of dimensionality  $D = 1$ , built up from small units of typical size  $R \approx 10 \text{ nm}$ . This behavior is quite revealing, as only few structures have a fractal dimension of unity. Among them are cylinders as the most prominent example; but also connected structures (e.g., toroids) can have fractal dimensions of unity.<sup>36</sup> A determination of structural invariants like molecular weights, radii of gyration and particle volumes from the scattering curves is complicated by the coexistence of several different particle structures, particle polydispersity, and particle inhomogeneity.

The scattering intensity is given by the sum of at least five contributions:

$$I(q) = I_{\text{sph}}P_{\text{sph}}(q) + I_{\text{frac}}P_{\text{frac}}(q) + I_{\text{mic}}P_{\text{mic}}(q) + I_{\text{mic}}P_{\text{mic}}(q) + I_{\text{fluc}}P_{\text{fluc}}(q) + I_{\text{mic}} \quad (6)$$

where “sph” indicates large globular structures, “frac” large self-similar structures, “mic” spherical micelles, “fluc” fluctuations around the average density profile in the corona, and “inc” the contribution due to incoherent scattering of the sample. Each contribution with the partial intensities  $I_i$  is given by

$$I_x = kc_x M_x \quad (7)$$

with the concentration  $c_x$ , the (weight-average) molecular weight  $M_x$ , and the ( $z$ -average) form factor  $P_x(q)$ .

**3.2. Limit of Low Salt Concentration.** At the lowest salt concentration ( $c_s = 0.001 \text{ mol/L}$ ,  $c_p = 6 \text{ g/L}$ ) the scattering intensity can be described by three contributions.

(1) *Large Globular Structures.* It is possible to describe their contribution to the scattered intensity with the form factor of a sphere  $P_{\text{sph}}$ . It is difficult to discriminate between different globular structures (solid spheres, ellipsoids, hollow spheres, vesicles), since only the Guinier region  $qR \leq 1$  is observed.

(2) *Spherical Micelles.* At intermediate to high  $q$ , the scattering curve reflects the core/shell structure of the micelles. Assuming the core to have a homogeneous density and the shell to exhibit a  $\phi(r) \sim r^{-a}$  density profile which is typical for spherical polymer brushes, the form factor is given by  $P_{\text{mic}}(q)$ .

(3) *Fluctuations.* At large  $q$  there is a noticeable weak decay into the base line. This can be due to either fluctuations around the average density profile in the micellar corona or to polyelectrolyte block copolymer unimers. However, because the critical micelle concentration of polyelectrolyte block copolymers is exponentially small,<sup>5</sup> their contribution to the scattered intensity should be negligible. In the respective  $q$  range, the scattering curve can be described by an infinitely thin cylinder  $P_{\text{cyl}}(q)$  having a  $q^{-1}$  asymptote indicating a locally stretched conformation of the polyelectrolyte chains in the corona.

The scattering curve at low salt concentrations can be analyzed by assuming the three terms  $I(q) = I_{\text{sph}}P_{\text{sph}}(q) + I_{\text{mic}}P_{\text{mic}}(q) + I_{\text{fluc}}P_{\text{fluc}}(q)$  to contribute to the total scattered intensity. The form factors  $P_x(q)$  are given in Table 1. Figure



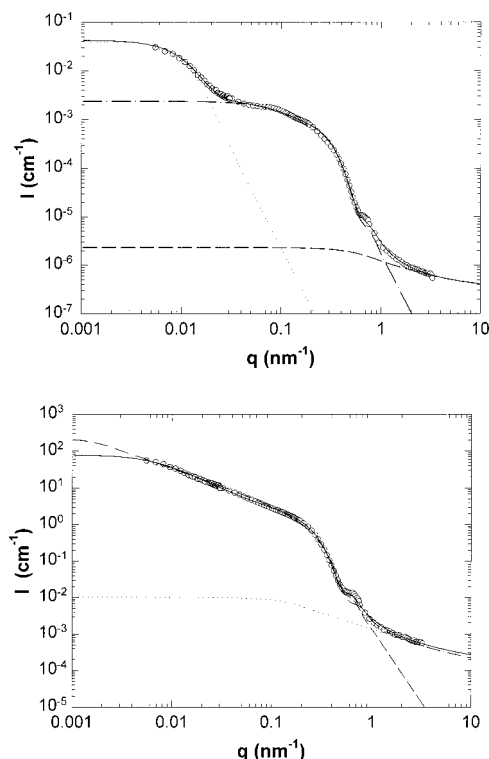


**Figure 3.** Contribution of each association structure to the total scattered intensity (—) at a polymer concentration of  $c_p = 6$  g/L for a salt-concentration of (a)  $c_s = 0.001$  mol/L and (b) 1 mol/L. In the low-salt case, large globules (···), micelles (·—), and fluctuations (—) contribute to the scattered intensity, whereas at high salt concentrations fractal networks (---) and fluctuations (···) dominate the scattering curve. Grey-filled symbols denote SLS data. Lines are nonlinear least-squares fits.

3a shows the contribution of each species to the total scattered intensity. The analysis yields the partial intensities  $I_{\text{sph}}$ ,  $I_{\text{mic}}$ , and  $I_{\text{fluc}}$ , the radius of the sphere  $R_{\text{sph}}$ , the micellar core radius  $R_c$ , and radius of gyration  $R_g$ , the fluctuation correlation length  $\xi$ , and the polydispersities  $\sigma_{\text{sph}}$  and  $\sigma_{\text{mic}}$ . The values are summarized in Table 2. Because the scattering curves are measured over a large  $q$ -range, each parameter can be determined with sufficient accuracy with the exception of the correlation length  $\xi$ , because the Guinier-regime of  $I_{\text{fluc}}(q)$  is dominated by the contribution of  $I_{\text{sph}}(q)$  and  $I_{\text{mic}}(q)$ .

At low salt concentrations, solution structures can be imaged with transmission electron microscopy (TEM). Figure 4 shows a transmission electron micrograph of micelles that had been cast from a dilute solution at a salt concentration of  $c_s = 0.001$  mol/L. The sample has been stained with uranyl acetate after solution casting. One observes the micellar cores as bright spherical domains surrounded by a thin dark layer of the micellar corona. The corona contrast is due to condensed ions ( $\text{NaCl}$ ,  $\text{UO}_2(\text{OAc})_2$ ). The average radii of the cores are 9–10 nm in good agreement with SANS experiments. Including the shell, the overall radius is 13–14 nm. It has so far not been possible to image solution structures at high salt concentrations because of artifacts induced by salt crystallization.

Taking the micellar core radius of  $R_c = 8.4$  nm at  $c_s = 0.001$  mol/L (Table 2) and assuming the micellar core to be a homogeneous PEE sphere, the aggregation number  $Z_{\text{mic}}$  can be calculated as

$$Z_{\text{mic}} = \frac{4\pi \rho_{\text{pee}} N_L R_c^3}{3 N_{\text{pee}} m_{\text{pee}}} \quad (8)$$

i.e.,  $Z_{\text{mic}} = 273$ . The concentration of micelles  $c_{\text{mic}}$  can be obtained from the intensity and contrast factor as  $c_{\text{mic}} = I_{\text{mic}}/kZ_{\text{mic}}M = 5.85$  g/L. From the remaining concentration  $c_{\text{sph}} = c - c_{\text{mic}} = 0.15$  g/L, one can estimate the aggregation number of large spherical particles as  $Z_{\text{sph}} = I_{\text{sph}}/kc_{\text{sph}}M = 191\,000$ , i.e., an aggregate consisting of the equivalent of 700 spherical micelles. It is likely that the globules have a vesicular structure. We recently reported the coexistence of spherical micelles and vesicles for a cationic polyelectrolyte block copolymer.<sup>37</sup>

**3.3. High Salt Concentrations.** At high salt concentrations, the scattered intensity is dominated by only two contributions arising from fluctuations and large structures with an intriguing  $I(q) \sim q^{-1}$  behavior over a large  $q$ -range. It is, however, not possible to consistently describe the scattering curve of the large structure with a cylinder as indicated in Figure 3b. It seems also unlikely that straight (nonbent) cylindrical aggregates of several  $\mu\text{m}$  length exist in solution. As the scattering curve cannot entirely be described by a particle of simple geometrical shape (sphere, cylinder, vesicle, disk), a meaningful and convenient parametrization can be achieved by assuming a general form of a self-similar aggregated structure built up from small spheres. The scattered intensity of such a structure is given by

$$P_{\text{frac}}(q) = [1 + N_{\text{frac}}P_s(q)]P_{\text{sph}}(q) \quad (9)$$

where  $P_s(q)$  is given in Table 1 and explained in the Appendix. The scattering curves can then be analyzed by assuming two contributions  $I(q) = I_{\text{frac}}P_{\text{frac}}(q) + I_{\text{fluc}}P_{\text{fluc}}(q)$ . Each contribution to the scattered intensity is shown in Figure 3b.

The analysis yields the partial intensities  $I_{\text{frac}}$  and  $I_{\text{fluc}}$ , the radius of gyration of the fractal aggregate  $R_g$ , the number of spheres in each aggregate  $N_{\text{frac}}$ , the fractal dimension  $d$ , and the correlation length  $\xi$ . Again, all parameters can be determined with sufficient accuracy with the exception of  $\xi$ . The values are summarized in Table 2. At intermediate salt concentrations the contribution of the large globular structures to the scattered intensity are considered as well.

**3.4. Salt-Dependence of Micellar Radii.** The micellar core radii  $R_c$  follow a systematic increase with increasing salt concentration and are independent of polymer concentration as shown in Figure 5: the addition of salt screens, the electrostatic repulsion of the corona chains, thereby decreasing the core/corona interfacial area  $b^2$  per chain. The area per chain  $b^2$  can be calculated from

$$b^2 = 4\pi \frac{R_c^2}{Z} \quad (10)$$

The aggregation number  $Z$  is obtained from the measured radius  $R_c$  with eq 8. The value of the grafting distance  $b$  are in the range 1.5–2.0 nm. Values are summarized in Table 2. One observes the expected systematic decrease of  $b$  with increasing salt concentration. Overall, charged systems have smaller grafting distances compared to uncharged systems ( $2 \leq b < 3$  nm).<sup>38,39</sup>

**3.5. Network Structures and Phase Separation.** Using dynamic scanning force microscopy (SFM), it is possible to image the solution structures in more detail. SFM has become an efficient tool in polymer and interface science to image individual macromolecular particles. It has been also used recently to investigate block copolymer micelles.<sup>40–42</sup> In the present case, micellar structures are adsorbed from highly dilute solutions (50 mg/L) onto different substrates (graphite, mica) and are imaged with SFM in the Tapping Mode. The reader is

**TABLE 2: Characteristic Parameters for Micellar Association Structures as Determined from the Analysis of the SLS/SANS-Curves for Different Polymer ( $c_p$ ) and Salt Concentrations ( $c_s$ )<sup>a</sup>**

$c_s$	(mol/L)	0.001	0.01	0.1	1.0	1.0	1.0	1.0
$c_p$	(g/L)	6.0	6.0	6.0	6.0	1.0	3.0	10.0
$I_{sph}$	(cm <sup>-1</sup> )	4000	3930			1040	2100	
$R_{sph}$	(nm)	220	232			263	270	
$\sigma_{sph}$		0.30	0.18			0.49	0.21	
$I_{frac}$	(cm <sup>-1</sup> )		158	170	214	44.5	130	209
$N_{frac}$			11.7	39.3	36.3		6.8	72.8
$R_{g,frac}$			204	296	307		147	322
$d$			1.82	1.71	1.58		1.73	1.86
$I_{mic}$	(cm <sup>-1</sup> )	237						
$R_{g,mic}$	(nm)	13.0						
$R_c$	(nm)	8.44	8.84	9.07	9.81	9.92	9.86	9.85
$\sigma_{mic}$		0.18	0.19	0.17	0.16	0.18	0.16	0.16
$I_{fluc}$	(cm <sup>-1</sup> )	0.20	0.59	0.32	1.0		0.15	0.29
$\xi$	(nm)	6.3	16.8	7.5	25.2		7.8	7.5
$M^{mic}$	(10 <sup>6</sup> g/mol)	5.94	6.84	7.36	9.32	9.64	9.45	9.43
$Z$		273	314	338	428	443	434	433
$b$	(nm)	1.81	1.77	1.75	1.68	1.67	1.67	1.68

<sup>a</sup>  $I$ ,  $R$ , and  $\sigma$  are the total scattered intensity, particle radius, and its relative standard deviation.  $N_{frac}$ ,  $R_g$ , and  $d$  are the number of spheres, the radius of gyration, and the fractal dimension of fractal aggregates.  $\xi$  is the correlation length of the fluctuations.  $M_{mic}$ ,  $Z$ , and  $b$  are the calculated micellar molecular weights, aggregation numbers, and grafting distances.

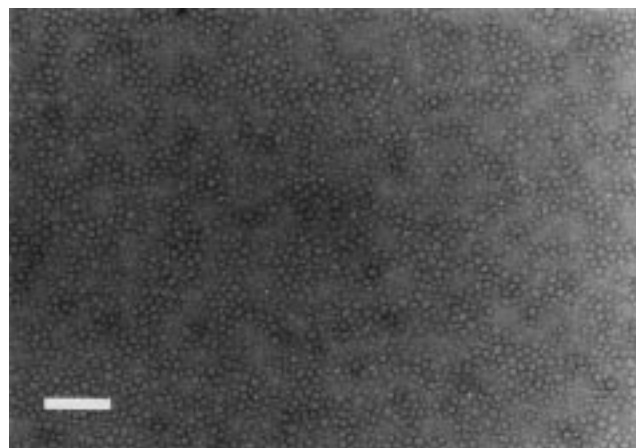


**Figure 4.** Transmission electron micrograph of micelles cast from a 0.01 mol/L solution. Micellar shells have been stained with uranyl acetate. Micellar cores have an average radius of  $R_c = 9.5$  nm; the collapsed corona has an average thickness of 2 nm. The scale bar is 200 nm.

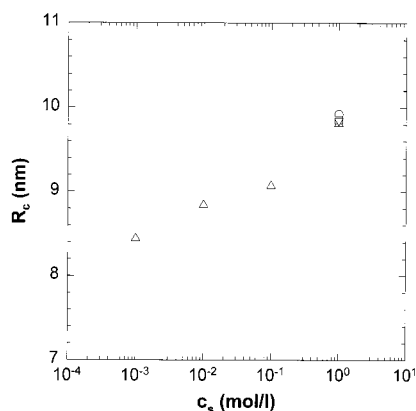


**Figure 5.** Increase of the measured core radius  $R_c$  with increasing salt concentration for  $c_p = 1$  (○), 3 (□), 6 (△), and 10 g/L (▽). The core radius is independent of the total polymer concentration.

referred to the subsequent paper in this issue for experimental details.<sup>25</sup> AFM-images of micellar structures at different salt concentrations are shown in Figure 6. At no added salt we observe spherical micelles (Figure 6a) with an average micellar radius of  $R_{AFM} = 20$  nm. This value is larger compared to the

values determined by electron microscopy ( $R = 14$  nm, Figure 4) which indicates moderate adsorption to the graphite substrate. Increasing the salt concentration to  $c_s = 0.05$  mol/L leads to the formation of wormlike micelles that exhibit a strong tendency to form crosslinks and loops or toroids. The toroids have diameters between 80 and 110 nm. Wormlike micelles and torus rims have a diameter of 27 nm, while the end caps have diameters of 40 nm, i.e., the same value as single spherical micelles. This is in agreement with the classical picture of micellization, where end caps of wormlike or cylindrical micelles are structurally similar to spherical micelles due to packing constraints. At an added salt concentration of  $c_s = 1$  mol/L, we observe the formation of large networks (Figure 6c). Electrostatic repulsion is almost totally screened, so that the networks adsorb so strongly to the substrate that they collapse. This makes a quantitative structural analysis nearly impossible. Only with block copolymers that have larger polyelectrolyte blocks like PEE(144)-PSSH(136), the network structures are stable enough to be imaged even at 1 M salt concentration (Figure 6d). This polymer exhibits the same aggregation behavior as PEE(114)-PSSH(83) and is investigated with AFM in more detail in the subsequent report.<sup>25</sup> The networks in Figure 6d consist of connected toroids forming large loops with diameters covering all length scales. This is a characteristic feature of self-similar structures, the most prominent one being the Sierpinski lattice that forms triangular holes on all length scales. The fractal dimension of the Sierpinski lattice is  $d_D = \log(D + 1)/\log(2)$  which is  $d_3 = 2$  in three dimensions ( $D = 3$ ). The values observed in our experiments are smaller (1.7–1.8, see Table 2), indicating a more “open” structure. Such kinds of fractal structures typically result from cluster–cluster aggregation, where typical fractal dimensions are in the range of  $1.80 \leq d \leq 2.09$  depending on the aggregation mechanism.<sup>43</sup> Monomer–cluster aggregation leads to larger fractal dimensions of  $2.50 \leq d \leq 3.0$ .

It is interesting to compare the observed association behavior to surfactants. Low molecular weight surfactants mostly form wormlike micelles instead of networks.<sup>44,45</sup> There have been some indications for network formation arising from an apparent decrease in radius of gyration with increasing concentration,<sup>46</sup> followed by a phase separation.<sup>47,48</sup> Networks are formed, if the energy of network junctions,  $E_{jct}$ , is smaller compared to the end-cap energy  $E_{cap}$ .<sup>49,50</sup> The relative values of both energies

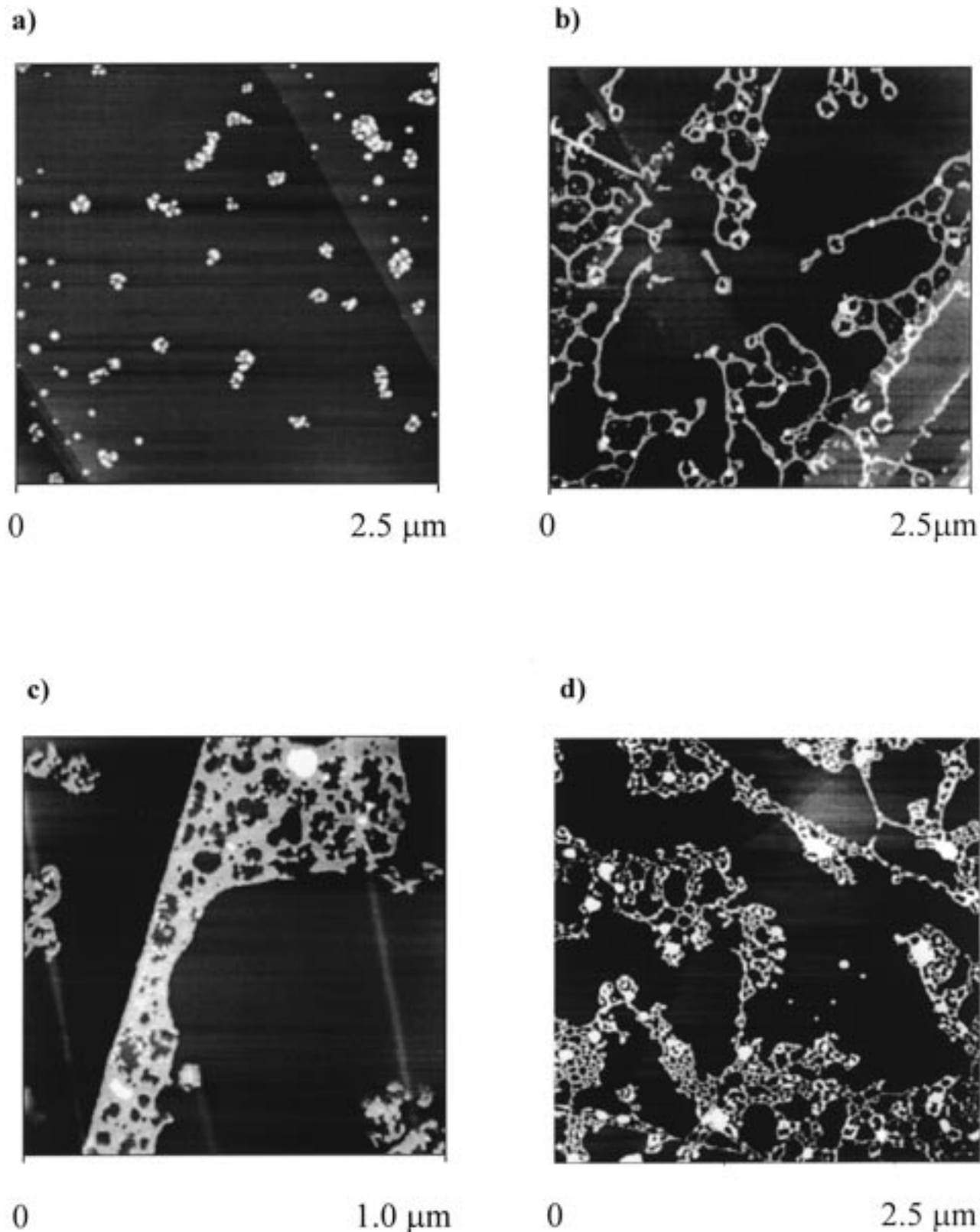


**Figure 6.** AFM images (height profile) of spherical micelles at (a) no added salt, (b) wormlike micelles exhibiting cross links, and loops at  $c_s = 0.05$  mol/L, and (c) collapsed micellar networks  $c_s = 1$  mol/L. The networks are more stable for block copolymers with longer polyelectrolyte blocks like for PEE(144)-PSSH(136) at (d)  $c_s = 1$  mol/L and consist of connected toroids forming a self-similar structure with large loops on all length scales.

seem to be the basic difference between low molecular weight surfactants ( $E_{\text{cap}} \ll E_{\text{jct}}$ ) and polyelectrolyte block copolymers ( $E_{\text{cap}} \gg E_{\text{jct}}$ ). The end-cap energies depend on salt concentration; an increase in salt concentration leads to higher end-cap energies, which is rationalized by a decrease in spontaneous curvature.

Generally, any factor that increases the end-cap energy decreases the cross-link energy, since in a cross link the spontaneous curvature changes in an opposite sense to that of the end-cap.

Increasing polymer concentration also increases the tendency to form network junctions. Within the mean-field description,

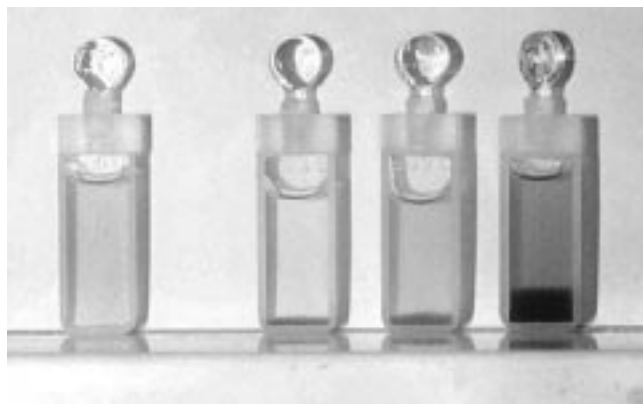


**Figure 7.** From left to right: solutions at concentrations of  $c_p = 10$ ,  $c_s = 1$  mol/L, and  $c_p = 5, 10, 25$  g/L,  $c_s = 3$  mol/L. Samples at high salt concentrations show phase separation into a dilute micellar solution and a concentrated viscous gel phase. The relative amount of gel phase is proportional to the polymer concentration.

the number of chain ends scales as  $X_1 \sim \phi^{1/2}$ , whereas the number of 3-fold and 4-fold junctions scale as  $X_3 \sim \phi^{3/2}$  and  $X_4 \sim \phi^2$ . Since the number of chain ends varies slowly, whereas the number of connections grows proportional to the polymer concentration, networks form.<sup>49</sup> Such network structures are parametrized by the arc-length density and cross-linking density. The first determines a geometrical mesh size with  $L_b$  defined as the arc length of the mesh or torus. The second fixes the typical arc-length  $L$  between cross links. The network structure is “saturated” if  $L = L_b$  and “unsaturated” if  $(L \gg L_b)$ . In this sense, the networks observed in Figure 6d are “unsaturated”.

Eventually, the formation of network junctions should lead to a phase separation into a dilute phase and a dense network phase. Such a macrophase separation is indeed observed at larger salt concentrations. Figure 7 shows one homogeneous sample at a salt concentration of 1 mol/L ( $c_p = 10$  g/L) and three phase separated samples at a salt concentration of 3 mol/L ( $c_p = 5, 10$ , and 25 g/L). The fraction of viscous gel phase increases proportional to the polymer concentration. The amber color of the solutions<sup>51</sup> corresponds in its intensity to the relative polymer concentrations in each of the phases. All phases are optically isotropic.

**3.6. Toroidal Structures.** AFM-images show networks consisting of connected loops or toroids. From the measured scattering curves  $I(q)$ , the presence of toroidal structure is not immediately apparent. As is often the case, the distance distribution function  $p(r)$  reveals more structural details. The distance distribution function is related to the correlation function  $\gamma(r)$  as  $p(r) = r^2\gamma(r)$ . The correlation function is obtained from Fourier inversion of the scattered intensity  $I(q)$

$$\gamma(r) = \frac{1}{2\pi^2} \int_0^\infty I(q) \frac{\sin(qr)}{qr} q^2 dq \quad (11)$$

The distance distribution functions for the scattering curves in Figure 2 are shown in Figure 8. The contribution of the large globular structures has been subtracted. A characteristic feature is the presence of two maxima at around  $r = 10$  nm and  $r = 100$  nm at large polymer and salt concentration. In Figure 9 the distance distribution functions of four common particle shapes (spheres, cylinders, toroid, vesicle) are compared. Only toroids exhibit two maxima at positions corresponding to the dimension of the rim and torus diameter. The average torus diameter of 100 nm as determined from the peak position in

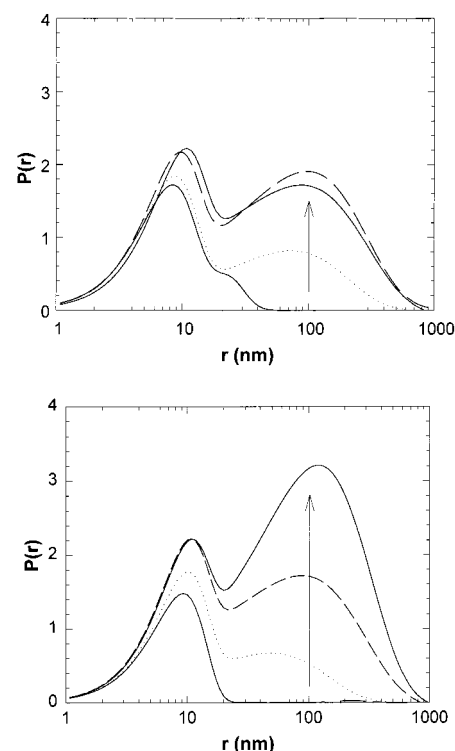


**Figure 8.** Measured distance distribution functions  $P(r)$  as a function of salt concentration  $c_s = 0.001$  (—),  $0.01$  (· · ·),  $0.1$  (— —), and  $1$  mol/L (····) at a polymer concentration of (a)  $c_p = 6$  g/L and for (b) different polymer concentrations  $c_p = 1$  (—),  $3$  (· · —),  $6$  (— —), and  $10$  g/L (····) at a salt concentration of (b)  $c_s = 1$  mol/L. Arrows indicate increasing (a) salt or (b) polymer concentration. With increasing ionic strength there is a build-up of correlations at a distance of  $r \approx 100$  nm indicating the fusion of micelles into larger association structures exhibiting a correlation length of 100 nm.

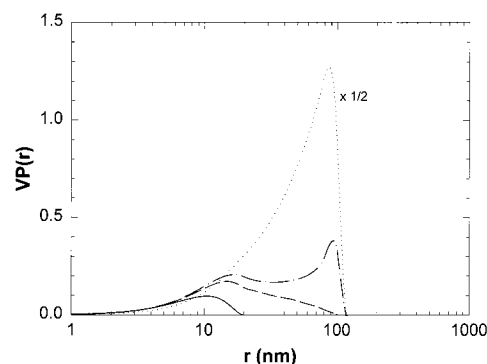


**Figure 9.** Calculated distance distribution functions  $P(r)$  for particles of simple shape multiplied by the particle volume  $V$  for a sphere with radius  $R = 10$  nm (—), a cylinder with radius  $R = 10$ , and length  $L = 100$  nm (— —), a torus with cross-sectional radius  $R_c = 10$  and overall radius  $R_t = 50$  nm (· · —), and a vesicle with radius  $R_v = 50$  nm and a thickness of 20 nm (····). Only the distribution function of a torus exhibits two separate peaks.

Figure 8 is in good agreement with the AFM-images (Figure 6b). In the measured distance distribution functions, the maximum corresponding to the torus diameter is smeared out due to the distribution of torus radii. In the Appendix it is shown that an ensemble of polydisperse toroids indeed leads to scattering curves as observed in Figure 2. Thus, the distance distribution functions show the growth of toroid-networks from spherical micelles with increasing polymer and salt concentration in good agreement with the results of the AFM studies. The shoulder at  $r \approx 20$  nm at the lowest salt concentration (Figure 8a) corresponds to the dimension of the micellar corona.



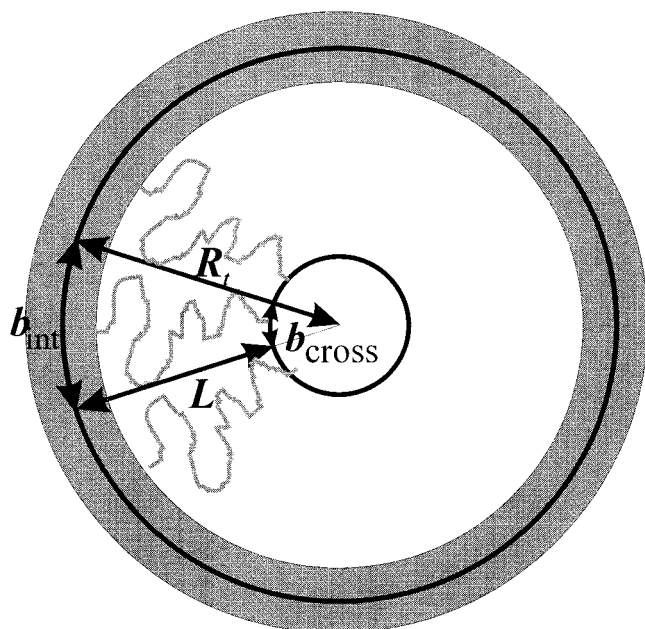


**Figure 10.** Simple model for the estimation of block copolymer torus or vesicle radii  $R_t$  from the grafting distance  $b$ , the effective polymer backbone diameter  $a$ , the average end-to-end distance  $L$ , and the core radius  $R_c$ . Inserting independently measured values for  $a$ ,  $b$ , and  $L$  leads to radii of 50–70 nm, similar to the values observed for toroids (present study) and vesicles.

The peak at a distance of about 100 nm corresponds to the mean diameter of the torus. This value is strikingly similar to the typical dimensions (100–150 nm) of block copolymer vesicles that had been recently observed.<sup>15,18,37</sup> The diameter and polydispersities of block copolymer vesicles are surprisingly small compared to vesicles formed by lipids, which can have diameters of several tens of  $\mu\text{m}$  at large polydispersities. There seems to be a thermodynamically preferred curvature radius of the order of  $R \approx 50$  nm for toroids ( $d = 1$ ) and vesicles ( $d = 2$ ). The curvature radius of a block copolymer torus or vesicle may be estimated using simple geometrical packing arguments. Such arguments have proven to be useful if thermodynamics is dominated by only two contributions: (1) the interfacial energy and (2) the stretching energy of the corona block. They have,

for example, been successfully applied to predict aggregation numbers of strongly segregated block copolymer micelles.<sup>38</sup> They allow to estimate the size of aggregate structures by using the average distance or grafting distance between two neighboring chains at the core/corona interface,  $b_{\text{int}}$ , the end-to-end distance  $L$  of the corona block, the cross-sectional diameter of a polymer chain  $b_{\text{cross}}$ , and the radius of the aggregate core  $R_c$ . For toroidal or vesicular aggregate structures this is illustrated in Figure 10.

The polyelectrolyte chains in the interior domain of the torus or vesicle are stretched to an end-to-end distance  $L$ . Using the geometry shown in Figure 10, the radius  $R_t$  of the torus or vesicle can be calculated from the grafting distance  $b_{\text{int}}$  and the effective chain cross-sectional diameter  $b_{\text{cross}}$  as

$$R_t = R_c + L \left( 1 + \frac{b_{\text{cross}}}{b_{\text{int}} - b_{\text{cross}}} \right) \quad (12)$$

In order to take into account effects of salt concentration, the chain cross-sectional diameter  $b_{\text{cross}}$  may be taken as a sum of a contribution of a bare diameter  $b_{\text{cross},0} \approx 0.5$  nm and an electrostatic contribution of the order of the Debye length, i.e.,  $b_{\text{cross}} = b_{\text{cross},0} + \kappa^{-1}$ . Using as a typical value  $L = 20$  nm, as determined from X-ray reflectivity of a planar PEE-PSSH-13 brush,<sup>52</sup> and taking the measured core radii and grafting distances (Table 2), calculated values of  $R_t$  are of the order of 50 nm at  $c_s = 1$  mol/L. The radius  $R_t$  in eq 12 has a pole at  $b_{\text{int}} = b_{\text{cross},0} + \kappa^{-1}$  where it diverges and changes its sign. The pole corresponds to a salt concentration of  $c_s \approx 0.05$  mol/L. Thus, below this salt concentration toroidal structures should become unstable. Experimentally, network structures disappear below  $c_s = 0.01$  mol/L. Vesicular structures may be stable at lower salt concentration because of a high concentration of condensed ions in the closed interior domain.

**3.7. Association of Polyelectrolyte Block Copolymers.** The observed association behavior of polyelectrolyte block copolymers exhibits many parallels to low molecular weight surfactants. With increasing spontaneous interfacial curvature, which can be caused by an increase of the alkyl chain length or an increase of salt concentration, surfactants form spherical micelles, wormlike micelles, or vesicles.<sup>53</sup> A similar trend is observed for polyelectrolyte block copolymers. However, instead

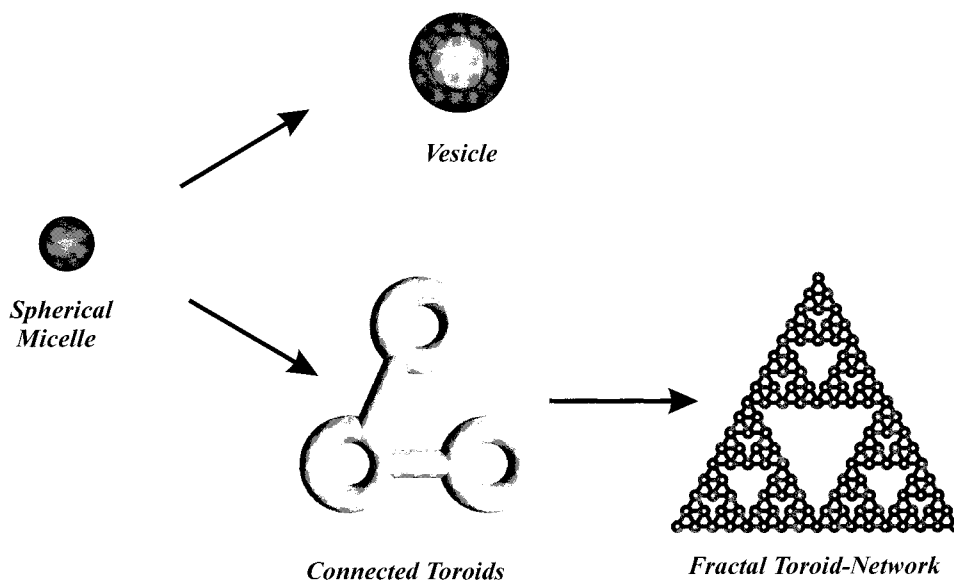


**Figure 11.** Schematic presentation of the association behavior of polyelectrolyte block copolymer micelles as inferred from this and related studies. With increasing ionic strength spherical micelles fuse into vesicles and networks consisting of looplike or toroidal structures.

of wormlike micelles, network structures are formed indicating the junction energy to be smaller than the end-cap energy. Networks are formed by increasing the polymer and salt concentration. In Figure 11, the association behavior of polyelectrolyte block copolymers as deduced from the present study, taking into account recent results on the formation of block copolymer vesicles,<sup>15,18,37</sup> is schematically illustrated.

At low salt and polymer concentrations, polyelectrolyte block copolymers form spherical micelles. There, the tendency to form associate structures is suppressed by electrostatic repulsion of the corona chains. Increasing salt concentration screens electrostatic repulsion and leads to the formation of structures or topologies with negative Gaussian curvature (junctions, toroids). Junctions connect toroid structures or loops to micronetworks and eventually lead to phase separation. Large micronetworks exhibit a fractal structure as a consequence of the association mechanism (cluster-cluster aggregation).

An unresolved question concerns the driving force for the formation of strongly bent structures (toroids, vesicles) with curvature radii of the order of only 50 nm. There are indications that charge effects play a major role in the formation of strongly bent polymeric structures. It is known that toroid formation can be induced for DNA by increasing polymer and salt concentration. As argued by Odijk et al.,<sup>54</sup> upon bending a charged cylinder, the effective potential will decrease because more counterions are attracted to the interior of the bent cylinder. This occurs concomitant with a charge renormalization<sup>55</sup> in the dense counterion region suppressing electrostatic repulsion. If the cylinder forms a torus, the space that is circumferenced by the torus represents a semidilute solution where the counterions can diffuse freely thereby gaining entropy. Such effects also seem to play a role in the stabilization of strongly curved structures formed by polyelectrolyte block copolymers.

The observation of network formation has some interesting implications for biological amphiphilic macromolecules like glycoproteins and proteoglycans. Proteoglycans consist of acidic polysaccharides (carboxylates or sulfates) covalently attached to hydrophobic core proteins. In aqueous solutions proteoglycans form viscous, jellylike solutions which are used to fill the space between tissue cells (mucous secretions) or act as the lubrication of skeletal joints (synovial fluid). Important to their performance is the formation of "self-healing" networks which structurally corresponds to the networks observed for polyelectrolyte block copolymers. The network junctions provide mechanical stability. In addition, destruction and spontaneous reformation of network junctions quickly dissipates frictional energy present in skeletal joints. Polyelectrolyte block copolymers may not only be a convenient model system to study structurally related network-properties but may even be a substitute in the case of tissue-damage.

#### 4. Conclusions

Polyelectrolyte block copolymers with large hydrophobic blocks form spherical micelles that fuse into networks and large globular structures with increasing polymer and salt concentration. The network structure could be elucidated with a combination of scattering (SLS, SANS) and microscopic techniques (AFM). It consists of connected loop-like structures (toroids). There is a preferred toroid radius of  $R_t \approx 50$  nm, set by geometrical packing requirements. Larger loops are formed at all length scales forming a self-similar fractal structure typical for diffusion limited aggregation. Apparently, network formation occurs via crosslinking of short cylindrical micelles, indicating that the end-cap energy is much larger than the cross-linking

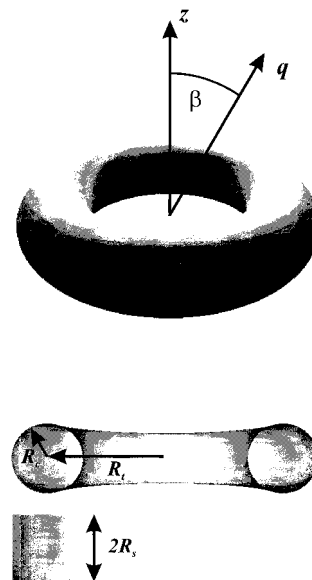


**Figure 12.** Characteristic parameters of a torus used for the calculation of the form factor  $P(q)$ .  $\beta$  is the angle between the  $z$  axis and the scattering vector  $q$ .  $R_t$  is the radius of the torus and  $R_c$  the cross-sectional radius.  $2R_c$  is the characteristic length of a torus with a square cross section.

energy for polymeric micelles. At large concentrations, cross-linking leads to macrophase separation into a dilute micellar phase and a highly swollen viscous phase.

**Acknowledgment.** We thank I. Below for help with the synthesis of the PS-PB block copolymer and P. van der Schoot for helpful discussions. Financial support of the German Science Foundation (Grant Fo246/2-1) and the Dr.-Hermann-Schnell foundation is gratefully acknowledged.

#### 5. Appendix

**5.1. Formfactor of Toroids.** Assuming the  $z$ -axis to point normal to the torus plane (Figure 12), the scattered amplitude  $F(q)$  is obtained by integrating over circular areas of constant phase shift at  $z = \text{const}$  from  $-R_c$  to  $R_c$

$$F(q, \psi) = \frac{1}{V} \int_{-R_c}^{R_c} \int_{R_t - \sqrt{R_c^2 - z^2}}^{R_t + \sqrt{R_c^2 - z^2}} \int_0^{2\pi} e^{-iq(z \cos \beta + r \sin \beta \cos \psi)} d\psi r dr dz \quad (\text{A.1})$$

where  $V = 2\pi^2 R_t^2 R_c$  is the volume of the torus with radius  $R_t$  and cross-sectional radius  $R_c$ . The integrations over  $\psi$  and  $r$  can be performed analytically to obtain

$$F_{\text{circ}}(q, \psi) = \frac{2\pi}{V} \int_{-R_c}^{R_c} [R_+ J_1(qR_+ \sin \beta) - R_- J_1(qR_- \sin \beta)] \frac{\cos(qz \cos \beta)}{q \sin \beta} dz \quad (\text{A.2})$$

with  $R_{\pm} = R_t \pm \sqrt{R_c^2 - z^2}$  and  $J_1(x)$  denoting the Bessel function. Integration over the angle  $\beta$  between the  $z$  axis and the scattering vector  $q$  yields the orientationally averaged form factor

$$P(q) = \int_0^{\pi/2} F^2(q, \psi) \sin \beta d\beta \quad (\text{A.3})$$

The calculation of the torus form factor involves two numerical integrations over  $z$  and  $\beta$ . A convenient approximation is to

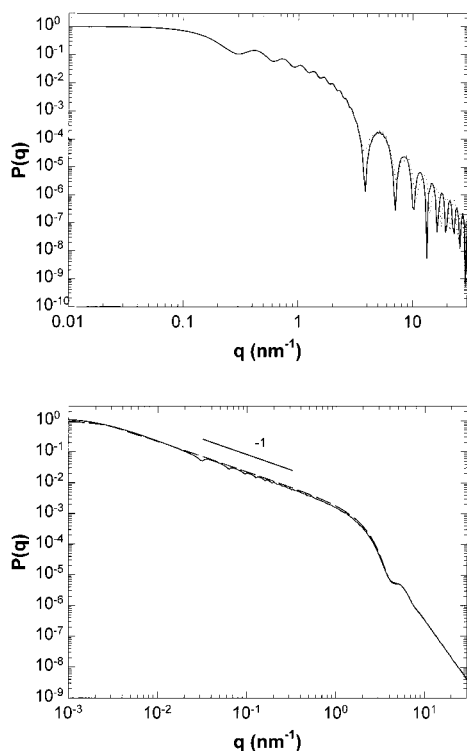


**Figure 13.** (a) Form factors  $P(q)$  of a torus with spherical (—) and square (···) cross section. In both cases the torus radius is  $R_t = 100$  nm. For comparison, cross-sectional radii are  $R_c = 10$  nm for the spherical and  $R_s = \sqrt{\pi}R_c/2$  for the square cross section to ensure identical volumes. There are characteristic oscillations with a  $q^{-1}$  envelope at intermediate  $q$  and oscillations with a Porod- $q^{-4}$ -envelope at high  $q$ . (b) A fractal size distribution of the torus radius overdamps oscillations at intermediate  $q$  (—) so that the scattering curve becomes nearly identical to the scattering curve of a cylinder (---) of the same cross-sectional radius and a cylinder length  $L = 1000$  nm. The relative standard deviation of the cross-sectional radius is  $\sigma = 0.16$ .

use a torus with a square cross section, i.e., a hollow cylinder with a length equal to the shell thickness  $2R$  (Figure 12). In this case the integration over  $z$  can be performed analytically. The form factor of a hollow cylinder has been calculated previously<sup>56</sup>

$$P_{sq}(q) = \int_0^{\pi/2} \frac{4 \sin^2(X_s \cos \beta)}{X_s^2 \cos^2 \beta} \left[ \frac{X_+ J_1(X_+ \sin \beta) - X_- J_1(X_- \sin \beta)}{(X_+^2 - X_-^2) \sin \beta} \right] \sin \beta d\beta \quad (\text{A.4})$$

with  $X_s = qR_s$ , and  $X_{\pm} = q(R_t \pm R_s)$ . The volume is  $V_{sq} = 8\pi R_s^2 R_t$ . In Figure 13a the form factor of a torus with cross-sectional radius  $R_c$  is compared to a torus with a square cross section with  $R_s = \sqrt{\pi}/2 R_c$  so that volumes are equal at given  $R$ . Both form factors exhibit damped oscillations with a  $q^{-1}$  envelope at intermediate  $q$  and a Porod  $q^{-4}$  envelope at large  $q$ .  $P_{sq}(q)$  exhibits superimposed high frequency oscillations in the Porod regime.

Polydispersity will significantly affect the scattering curve. The averaged form factor is obtained by integrating over a size distribution function  $h(R)$

$$\langle P(q) \rangle_z = \int_0^\infty P(q, R) h(R) dR \quad (\text{A.5})$$

A convenient particle size distribution is the Schulz–Zimm

distribution

$$h_{sz}(R) = \frac{(z+1)^{z+1} R^z}{\langle R \rangle^{z+1} \Gamma(z+1)} \exp \left[ -\frac{(z+1)R}{\langle R \rangle} \right] \quad (\text{A.6})$$

$\langle R \rangle$  is the average radius and  $z$  the polydispersity index which is related to the relative standard deviation through  $\sigma = (z+1)^{-1/2}$ . The distribution is normalized such that  $\int_0^\infty h(R) dR = 1$ .

**5.2. Structure Factor of Fractal Aggregates.** The scattering of fractal aggregates is usually obtained by convoluting the interparticle distance distribution function  $P_s(r)$  describing the fractal aggregation structure with the intraparticle distance distribution function  $P_i(r)$ , e.g., that of a sphere. In Fourier space this yields the scattering intensity as a simple product of  $P_s(q)P_i(q)$ .

The form factor of fractal aggregates with fractal or Hausdorff dimension  $d$  is given by the Fourier transform of a segment distribution function

$$P_s(r) = \frac{B}{r^3} \left( \frac{r}{R_g} \right)^d \exp \left[ -C \frac{r}{R_g} \right] \quad (\text{A.7})$$

where the coefficients  $B$  and  $C$  are determined by the requirements  $\int_0^\infty P(r) 4\pi r^2 dr = 1$  and  $\int_0^\infty r^2 P(r) 4\pi r^2 dr = R_g^2$  as  $B = (C^d)/(4\pi\Gamma(d))$  and  $C = (d(d+1))^{1/2}$ . The radius of gyration  $R_g$  is related to the upper cutoff distance of the fractal size distribution  $\xi$  by  $\xi^2 = R_g^2/C^{57}$ , where the cutoff is taken to be exponential, i.e., of the form  $e^{-r/\xi}$ . The form factor  $P_s(q)$  can be obtained by Fourier transform

$$P_s(q) = \int_0^\infty P(r) \frac{\sin(qr)}{qr} 4\pi r^2 dr = \frac{\sin[(d-1) \arctan(X)]}{X(d-1)[1+X^2]^{(d-1)/2}} \quad (\text{A.8})$$

with  $X = qR_g/C$ . This function has been used to analyze scattering curves of fractal objects.<sup>57,58</sup> The product of  $P_s(q)$  with the form factor of spheres adequately describes the measured scattering functions in Figure 2 and can be used to parametrize  $I(q)$  for the calculation of the distance distribution function. In view of Figure 11, the fractal aggregate may alternatively be described as an ensemble of toroids having a fractal distribution of torus diameters  $R_t$ . The scattering intensity may then be calculated by averaging over the fractal size distribution of the form  $h_{\text{frac}}(R) = P_s(r)$ , i.e.

$$\langle P(q) \rangle = \int_0^\infty \int_0^\infty P(q, R_t, R_c) h_{\text{frac}}(R_t) h_{sz}(R_c) dR_c dR_t \quad (\text{A.9})$$

$h_{sz}(R)$  is the Schulz–Zimm distribution for the torus cross-sectional diameter. In Figure 13b the form factor of such an ensemble of toroids with square cross section  $R_s = 8.86$  nm, a fractal size distribution with a radius of gyration  $R_g = 5000$  nm and fractal dimension  $d = 2$ , is shown. A relative standard deviation  $\sigma_c = 0.16$  of the torus cross-sectional radius leads to damping of the oscillations in the Porod regime. The fractal size distribution nearly smears out oscillations in the intermediate  $q$  regime  $h_{\text{frac}}(R_t)$  leaving the  $q^{-1}$ -envelope. The form factor can be compared to a cylinder of radius  $R_c = 10$  nm, length  $L = 10000$  nm, and the same standard deviation of the cylinder cross section. If the torus oscillations in the intermediate  $q$  regime are completely smeared out, the scattering curves are practically identical except at low  $q$ , where, depending on the

fractal dimension, the torus exhibits a slight overshoot of the scattered intensity.

## References and Notes

- (1) Tuzar, Z.; Kratochvil, P. *Adv. Colloid Interface Sci.* **1976**, *6*, 201.
- (2) Tuzar, Z.; Kratochvil, P. In *Surface and Colloid Science*; Matijevic, E., Ed.; Plenum Press: New York, 1993; Vol. 15.
- (3) Selb, J.; Gallot, Y. *Developments in Block Copolymers*, 2nd ed.; Goodman, I., Ed.; Elsevier: Amsterdam, 1985.
- (4) Tuzar, Z. In *Solvents and Self-Organization of Polymers*; Webber, S. E., Munk, P., Tuzar, Z., Eds.; NATO ASI Series E 327; Kluwer: Dordrecht, Netherlands, 1996.
- (5) Moffitt, M.; Khougaz, K.; Eisenberg, A. *Acc. Chem. Res.* **1996**, *29*, 95.
- (6) Tian, M.; Qin, A.; Ramireddy, C.; Webber, S. E.; Munk, P.; Tuzar, Z.; Prochazka, K. *Langmuir* **1993**, *9*, 1741.
- (7) Zhang, L.; Shen, H.; Eisenberg, A. *Macromolecules* **1997**, *30*, 1001.
- (8) Yu, Y.; Zhang, L.; Eisenberg, A. *Macromolecules* **1998**, *31*, 1144.
- (9) Cao, T.; Munk, P.; Ramireddy, C.; Tuzar, Z.; Webber, S. E. *Macromolecules* **1991**, *24*, 6300.
- (10) Prochazka, K.; Kiserow, D.; Ramireddy, C.; Tuzar, Z.; Munk, P.; Webber, S. E. *Macromolecules* **1992**, *25*, 454.
- (11) Kiserow, D.; Prochazka, K.; Ramireddy, C.; Tuzar, Z.; Munk, P.; Webber, S. E. *Macromolecules* **1992**, *25*, 461.
- (12) Tian, M.; Qin, A.; Ramireddy, C.; Webber, S. E.; Munk, P.; Tuzar, Z.; Prochazka, K. *Langmuir* **1993**, *9*, 1741.
- (13) Gao, Z.; Varshney, S. K.; Wong, S.; Eisenberg, A. *Macromolecules* **1994**, *27*, 7923.
- (14) Zhang, L.; Barlow, R. J.; Eisenberg, A. *Macromolecules* **1995**, *28*, 6055.
- (15) Zhang, L.; Eisenberg, A. *Science* **1995**, *268*, 1728.
- (16) Yu, K.; Zhang, L.; Eisenberg, A. *Langmuir* **1996**, *12*, 5980.
- (17) Yu, Y.; Zhang, L.; Eisenberg, A. *Langmuir* **1997**, *13*, 2578.
- (18) Zhang, L.; Yu, K.; Eisenberg, A. *Science* **1996**, *272*, 1777.
- (19) Zhang, L.; Eisenberg, A. *J. Am. Chem. Soc.* **1996**, *118*, 3168.
- (20) Valint, P. L.; Bock, J. *Macromolecules* **1988**, *21*, 175.
- (21) Guenoun, P.; Lipsky, S.; Mays, J. W.; Tirrell, M. *Langmuir* **1996**, *12*, 1425.
- (22) Guenoun, P.; Davis, H. T.; Tirrell, M.; Mays, J. W. *Macromolecules* **1996**, *29*, 3965.
- (23) Huang, C.; Olvera de la Cruz, M.; Delsanti, M.; Guenoun, P. *Macromolecules* **1997**, *30*, 8019.
- (24) Guenoun, P.; Delsanti, M.; Gazeau, D.; Mays, J. W.; Cook, D. C.; Tirrell, M.; Auvray, L. *Eur. Phys. J. B* **1998**, *1*, 77.
- (25) Regenbrecht, M.; Akari, S.; Förster, S.; Möhwald, H., *J. Phys. Chem. B* **1999**, *103*, 6669.
- (26) Young, R. N.; Quirk, R. P.; Fetters, L. J. *Adv. Polym. Sci.* **1984**, *56*, 1.
- (27) Auschra, C.; Stadler, R. *Polym. Bull.* **1993**, *36*, 257.
- (28) Thaler, W. A. *Macromolecules* **1983**, *16*, 623.
- (29) Vink, H. *Makromol. Chem.* **1981**, *182*, 279.
- (30) Förster, S.; Schmidt, M. *Adv. Polym. Sci.* **1995**, *120*, 51.
- (31) Förster, S.; Schmidt, M.; Antonietti, M. *Polymer* **1990**, *31*, 781.
- (32) Lindner, P. In *Modern Aspects of Small-Angle Scattering*; Brumberger, H., Ed.; NATO Advanced Study Institutes, Ser. C 451; Kluwer Academic, London, 1993.
- (33) Förster, S.; Burger, C. *Macromolecules* **1998**, *31*, 87.
- (34) Daoud, M.; Cotton, J. P. *J. Phys. (Paris)* **1982**, *43*, 531.
- (35) Förster, S.; Wenz, E.; Lindner, P. *Phys. Rev. Lett.* **1996**, *77*, 95.
- (36) Borisov, O. V.; Vilgis, T. A. *Europhys. Lett.* **1996**, *35*, 327.
- (37) Krämer, E.; Förster, S.; Göltner, C.; Antonietti, M. *Langmuir* **1998**, *14*, 2027.
- (38) Förster, S.; Zisenis, M.; Wenz, E.; Antonietti, M. *J. Chem. Phys.* **1996**, *104*, 9956.
- (39) Förster, S.; Hermsdorf, N.; Böttcher, C.; Lindner, P. Submitted for publication.
- (40) Spatz, J. P.; Roescher, A.; Sheiko, S.; Krausch, G.; Möller, M. *Adv. Mater.* **1995**, *7*, 731.
- (41) Li, Z.; Zhao, W.; Liu, Y.; Rafailovich, M. H.; Sokolov, J.; Khougaz, K.; Eisenberg, A.; Lennox, R. B.; Krausch, G. *J. Am. Chem. Soc.* **1996**, *118*, 10892.
- (42) Meiners, J. C.; Quintelritzi, A.; Mlynek, J.; Elbs, H.; Krausch, G. *Macromolecules* **1997**, *30*, 4945.
- (43) Schäfer, D. W. *Science* **1989**, *243*, 1023.
- (44) Cates, M. E.; Candau, S. J. *J. Phys.: Condens. Matter* **1990**, *2*, 6869.
- (45) Hoffmann, H. *Adv. Colloid Interface Sci.* **1990**, *32*, 123.
- (46) Kathory, A.; Lequeux, F.; Kern, F.; Candau, S. J. *Langmuir* **1993**, *9*, 1456.
- (47) Appel, J.; Porte, G. *J. Phys. Lett. (France)* **1983**, *44*, L689.
- (48) Porte, G.; Gomati, R.; El Haitamy, O.; Appell, J.; Marignan, J. J. *Phys. Chem.* **1986**, *90*, 5746.
- (49) Elleuch, K.; Lequeux, F.; Pfeuty, P. *J. Phys. (Paris)* **1995**, *5*, 465.
- (50) Drye, T. J.; Cates, M. E. *J. Chem. Phys.* **1992**, *96*, 1367.
- (51) The color, which is the typical color also known from ion exchange resins, is due to traces (<0.1%) of oxidation products upon sulfonation.
- (52) Ahrens, H.; Förster, S.; Helm, C. A. *Macromolecules* **1997**, *30*, 8447.
- (53) Seddon, J. M. *Biochim. Biophys. Acta* **1990**, *41*, 525.
- (54) Ubbink, J.; Odijk, T. *Biophys. J.* **1995**, *68*, 54.
- (55) Alexander, S.; Chaikin, P. M.; Grant, P.; Morales, G. J.; Pincus, P.; Hone, D. *J. Chem. Phys.* **1984**, *80*, 5776.
- (56) Mittelbach, P.; Porod, G. *Acta Phys. Austriaca* **1961**, *14*, 405.
- (57) Sorensen, C. M.; Cai, J.; Lu, N. *Langmuir* **1992**, *8*, 2064.
- (58) Chen, S.-H.; Teixeira, J. *Phys. Rev. Lett.* **1986**, *57*, 2583.